Chapter 6

HIGH-CONTRAST GRATINGS

Metamaterials are arrangements of more than one natural material at a small enough size scale that they combine to create a new effective medium with properties distinct from the components. This is most exciting when resultant properties are inaccessible with natural materials. Recently, metasurfaces, 2-dimensional metamaterials, have received much attention as an easy-to-fabricate subset of metamaterials, which still enable extraordinary properties including near-unity reflectance [39] and zero backscattering [40]. The generalization of Snell's Law to include phase discontinuities imparted by subwavelength scale interface features creates a framework for designing laterally macroscopic optics with sub-optical wavelength thicknesses [41].

My work has focused on a type of metasurface that has also been referred to as a high-contrast grating (HCG), which is the term I will use in this chapter. HCG, shown schematically in Figure 6.1a, are composed of a layer of high-refractive index semiconductor material patterned at a near-subwavelength size scale. That is, the characteristic length of the grating lies between $\frac{\lambda_0}{n_g}$ and $\frac{\lambda_0}{n_{med}}$, where the refractive index of the grating material is high and the refractive index of the grating medium. (Based on the following results and realistically accessible materials, I say $n_g \geq 3$ and $n_{med} \leq 1.55$.) These structures have been shown as a viable replacement to Bragg reflectors in Vertical Cavity Side Emitting Lasers thanks to their broadband, single polarization reflectivity [42]. Patterned crystalline silicon on a glass substrate was shown to have 74% peak reflectivity at normal incidence with >40% reflectivity at a 45° angle for use in color filters for displays. [43] The same group also demonstrated fabrication of their grating designs by nano-imprint lithography achieving 85% peak reflectivity centered at 620 nm for their red color filter. [44] Another group reported simulation results with polarization independent HCG reflectivity above 99% at normal incidence using crossed silicon stripes suspended in air which could be achieved by undercut etching.

The mechanism for high reflectivity is proposed to be modal interference within the grating layer preventing light from transmitting through. Since the subwavelength scale of the features renders non-0th diffracted orders evanescent, specular back-

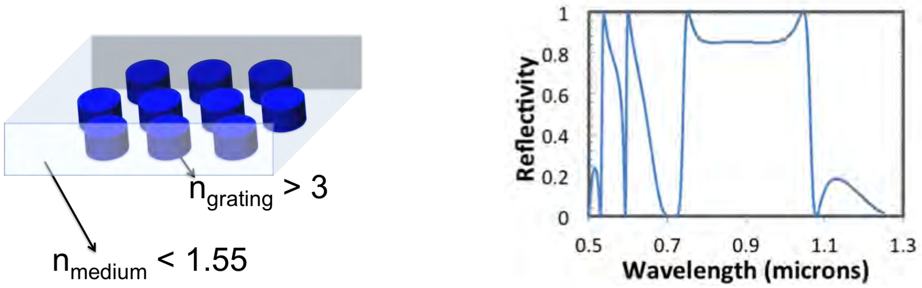

(a)

(b)

Figure 6.1: (left) High-contrast grating schematic and (right) top-hat reflection profile of a simulated high-contrast grating.

reflection can go to near unity [45]. Reference [46] considers the grating layer as simultaneously a homogenized effective medium and a coupler for light into the homogenized effective medium. They identify the modes at work to be the Fabry-Perot resonance and the guided modes of the effective medium layer. The slowly varying Fabry-Perot resonance and the quickly varying waveguide mode interfere, producing a Fano resonance. The next higher order waveguide mode also interferes with the Fabry-Perot mode producing a Fano resonance with the opposite arrangement of its sharp and slow cut-offs. These two adjacent Fano resonances with opposite alignment give a top-hat like reflection profile which is exactly the desired characteristic for a band-stop filter. An example is shown in Figure 6.1b. Since the coupling into the guided waveguide mode is through the grating vector $\boldsymbol{G} = \frac{2\pi}{Period}$, as the incident angle deviates from normal, the lowest order coupling via diffracted orders ± 1 splits, since the ± 1 orders are no longer degenerate at non-normal incidence angles. Reference [47] demonstrated that the degree of symmetry of the tiling of grating elements is an important design characteristic of the gratings for the response of different polarization light and for more uniform performance with varying incident angle. A HCG based spectrum-splitting optic has been designed [48] with a test filter demonstrated for a Cassegrain device architecture [49]. A fabricated TiO_2 grating (with low refractive index contrast) showed poor performance relative to the designed specifications, and side-wall angles were found to be a sensitive parameter with deviations of just a couple of degrees from 90° sidewalls, giving large drop-offs in performance.

As described in Chapter 5, the main cost driver for a high efficiency design of the Polyhedral Specular Reflector spectrum-splitting design, detailed in Chapter 3, is the dichroic filter fabrication. High-contrast gratings are a promising alternative

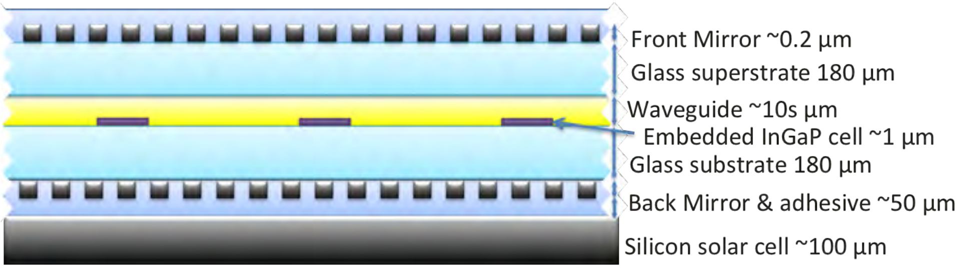

Figure 6.2: Spectrum splitting applications of high-contrast gratings include (right) Polyhedral Specular Reflector and (left) Tandem Luminescent Solar Concentrator.

for the splitting elements for cost and complexity reduction. In contrast to the slow fabrication process to deposit many-micron-thick distributed Bragg reflectors (DBR), the grating features can be made by a single sub-micron layer deposition followed by nanoimprint lithography and an etching processes, which can be done at large volumes. Additionally, sub-micron thicknesses mean less material per filter compared to a DBR. By virtue of the high refractive index contrast, the reflection band of HCG can also be more incident-angle tolerant. The requirement of many layers of materials and for material compatibility among successive DBR layers limits the use of layers with very different refractive index (e.g. ten pairs of GaP and SiO_2). Using HCG allows fewer components and less material per unit aperture area in a spectrum-splitting solar device, reducing cost and complexity. Figure 3.1e shows a schematic of the PSR in which the filters would be HCG. Early results on HCG showed a remarkable degree of angle insensitivity which prompted us to explore an additional application of HCG as a spectrum-splitting optical element in a Tandem Luminescent Solar Concentrator (TLSC) shown in Figure 6.2.

Tandem Luminescent Solar Concentrator

A luminescent solar concentrator (LSC) is a device which exploits the ability to expend energy to decrease entropy of light. This trade-off allows concentration of diffuse light, which without the energy trade-off violates the second law of thermodynamics. The definition of free energy, $\Delta G = \Delta H - T\Delta S \leq 0$, gives the minimum ΔH required to decrease the entropy of diffuse sunlight. Thus, solar light can be collected from a wide range of angles and downshifted by a dye or, as in our case, quantum dots. The photoluminescence of the quantum dots is trapped within a waveguide that has an aperture area of active semiconductor material which can collect the concentrated light. This collection aperture area is smaller than total input area of sunlight, implying a certain geometric concentration ratio. Traditional

LSC only use total internal reflection (TIR) to trap luminescence. Photoluminescent light hitting the front and back interfaces of the device are reflected back if the angle of incidence is beyond the critical angle as defined by Snell's law. Any light within the escape cone is lost. Traditional LSC thus have large losses and low efficiency.

Our strategy is to sandwich the quantum dot embedded waveguide between two bandstop mirrors with high reflectivity in the photoluminescence range and high transmission everywhere else to trap the photoluminescence in the waveguide. Shorter wavelength light will be transmitted through the top mirror into the waveguide, absorbed by the quantum dots, downshifted, and trapped by the mirrors. Longer wavelengths of light will be transmitted through both top and bottom mirrors to an underlying silicon solar cell. This tandem architecture has the potential to improve upon the efficiency of a silicon solar cell by converting higher energy photons in a cell which generates greater voltage. In executing this project, we will use near-unity CdS/CdSe core/shell quantum dots from the group of Paul Alivisatos at UC Berkeley and high-quality InGaP cells from the NREL III-V group.

Filter Specifications

Ideal filters for the PSR would have on average >85% reflectivity within the target band and >90% transmission for longer wavelengths. High transmission for longer wavelengths is important, since erroneously transmitted photons can still be converted in a lower bandgap cell but erroneously reflected light is lost completely in a higher bandgap cell. The seventh filter is a metallic mirror coated with a few dielectric layers to give full broadband reflectivity. However, to give shorter wavelength light a second chance to be absorbed in the following cell rather than the lowest, longpass rather than band stop filters would be most ideal for this design. Figure 6.3 shows the target specs for each of the seven PSR filters and TLSC mirrors vertically offset with the high values showing regions for which unity reflectivity is desired and the low value for each trace corresponding to zero reflectivity. The lighter colored portion of the trace for Filter bands 2 through 7 and TLSC Bottom shows the region in which the filter performance is non-critical though the indicated performance would be beneficial.

For the LSC application, the top and bottom mirrors have slightly different requirements. For the top mirror, the target is to let in as much light as possible while still maintaining high reflectivity at the peak of quantum dot photoluminescence to allow in as much incident power as possible. The back mirror target is slightly

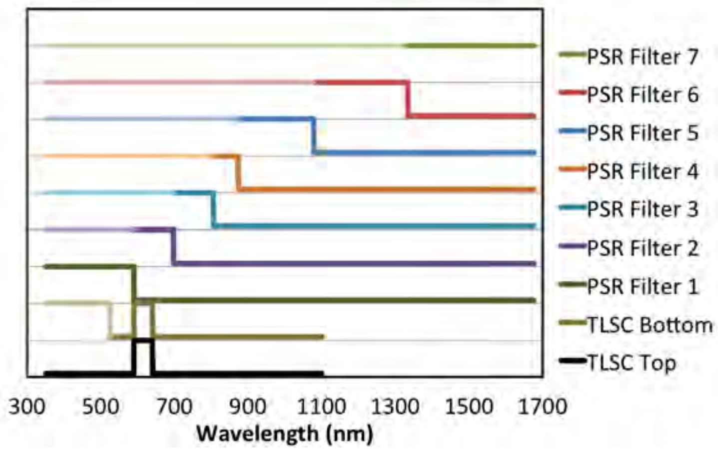

Figure 6.3: Target specifications for filters for the Polyhedral Specular Reflector and Tandem Luminescent Solar Concentrator.

more complex. The quantum dots absorb short wavelength light up to around 525 nm. The photoluminesced light peaks near 615 nm and has a bandwidth of about 50 nm. Thus the power in the spectrum between 525 nm and 590 nm light should pass through the back mirror to the underlying silicon cell. This is a high power portion of the spectrum, so failure to collect light in this spectral region would be detrimental. Additionally, high reflectivity for the short wavelength light absorbed by the quantum dots would allow it to pass through the waveguide twice. This dual pass absorption allows either improved absorption of the light toward the absorption edge of the quantum dots, i.e. just below 525 nm where the dot absorption is weaker, or allows the optical density of the waveguide to be as low as half of what it would need to be for full absorption in a single pass. This design freedom is advantageous but not required for high performance, and thus this portion of the bottom mirror filter specification is also a "want" rather than a "need".

6.1 High-contrast grating modeling

High-contrast grating modeling was done using the rigorous coupled wave analysis (RCWA) method [50] using commercial software program RSoft DiffractMOD. With this semi-analytical method, the steady state electric fields from plane wave illumination of an infinitely periodic, planar grating can be determined. The periodic, complex dielectric function of the grating layer is expressed as a Fourier series truncated to a finite number of terms. The electric fields in the grating layer and the media on either side of the infinite layer are represented as sums over the same series terms. Applying boundary conditions of Maxwell's equations at the interfaces be-

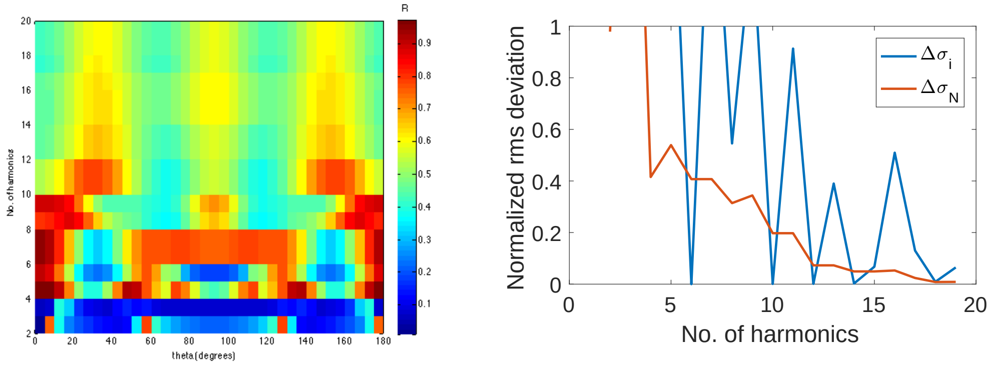

(a) (b)

Figure 6.4: Example of convergence testing simulation data (right) and (left) results of applying normalized rms deviation metric.

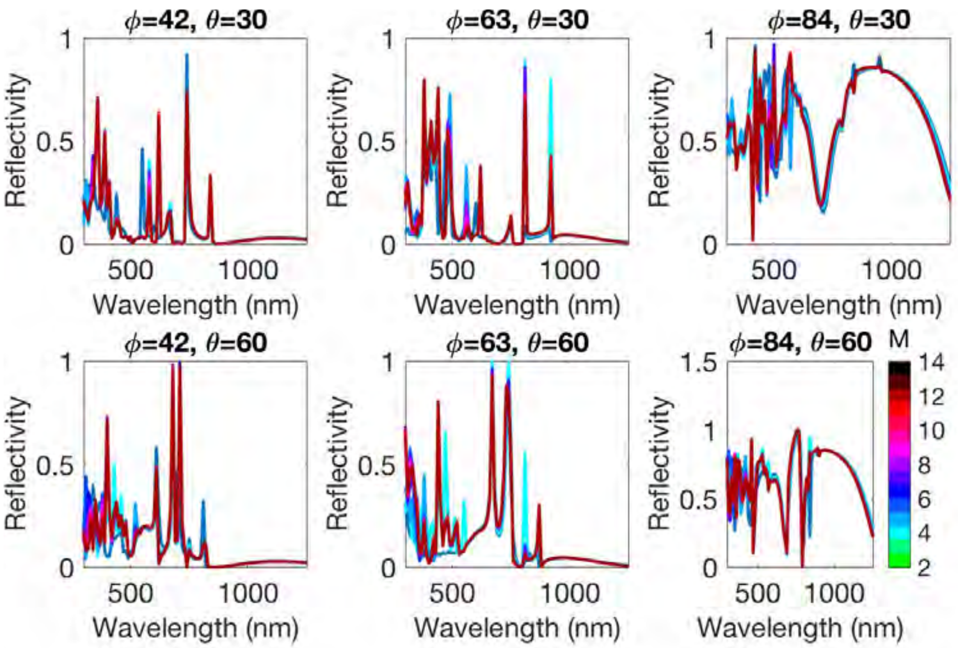

Figure 6.5: Broadband and multiple angle convergence testing results for n=2.7 grating in n=1.5 medium.

tween the grating and the incident and transmitting media gives a series of coupled equations which can be solved by a numerical matrix inversion, giving steady-state fields in all space. Related quantities such as transmission, reflection, absorption, and intensity in each diffracted order can be calculated from this. This method is faster than a full numerical solution to time-dependent Maxwell's equations.

The accuracy of RCWA simulations and the required computational time depend

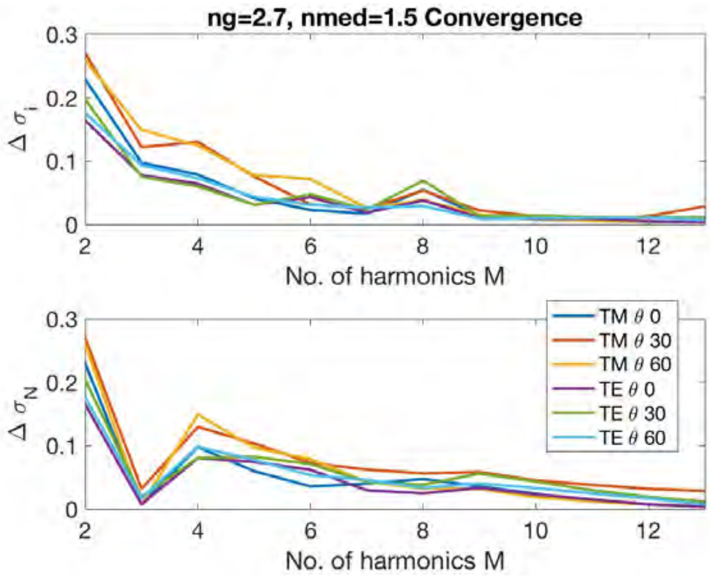

Figure 6.6: Normalized rms deviation of reflectivity of n=2.7 grating in n=1.5 medium.

on the number of Fourier terms, or harmonics. Convergence testing is required to obtain the appropriate number of harmonics for sufficiently accurate results. Simulations always give some answer. It is up to the modeler to evaluate whether the results are meaningful or not. Figure 6.4a shows a clear example of what can go wrong. These data show the reflectivity of TM polarization light from a grating composed of silicon nanopillars, hexagonally tiled with air as the grating medium. The wavelength $\lambda_0 = 600\ nm$, and polar angle of incidence $\phi = 30°$ with azimuthal angle θ ranging from 0° to 180° by 5° increments. The reflectivity is plotted as a function of the number of harmonics (from 2 to 20) included in the calculation. It is clear from this that simulations at a small number of harmonics significantly misconstrue grating reflectivity. Around twelve to fourteen harmonics the 60° rotational symmetry of the lattice becomes apparent.

In order to quantify the discrepancy and set a threshold for what level of variation is acceptable I use a pair of normalized root mean squared (rms) error metrics, defined as

$$\Delta\sigma_i = \sqrt{\frac{\sum_j \left(R_{i+1}(\lambda_j) - R_i(\lambda_j)\right)^2}{\sum_j R_i^2(\lambda_j)}} \tag{6.1}$$

$$\Delta\sigma_N = \sqrt{\frac{\sum_j \left(R_N(\lambda_j) - R_i(\lambda_j)\right)^2}{\sum_j R_i^2(\lambda_j)}}, \tag{6.2}$$

where $\Delta\sigma_i$ is the rms deviation between the results for i harmonics versus $i + 1$ harmonics, and $\Delta\sigma_N$ is the deviation between the results for i harmonics and N harmonics with N being a large number which is assumed to give fairly accurate results. The values of $\Delta\sigma_i$ and $\Delta\sigma_N$ for this case plotted in Figure 6.4b show that the value of $\Delta\sigma_i$ has not stabilized even for a large number (10-20) of harmonics, however, the relative error from $harmonics = 20$ drops below about 10% starting with harmonics=12. In general, as the ratio of wavelength to grating periodicity decreases, more harmonics are necessary. Thus for the broadband simulations necessary for spectrum splitting optical elements, I have done broadband convergence testing. An example is shown in Figure 6.5 where for different values of polar angle ϕ and azimuthal angle θ, reflection spectra are shown calculated using a range of number of harmonics. It is clear that the values change more as a function of the number of harmonics for shorter wavelengths. Smaller numbers of harmonics also produce some artificial resonances. Applying Equations 6.1 and 6.2 to these results yields Figure 6.6 indicating relative errors below 5% for ten or more harmonics. As seen in Figure 6.4a, however, plateaus in results do occur for certain numbers of harmonics, so it would be safer to additionally compare a subset of the results, to a simulation done with a much larger number of harmonics as well.

6.2 Results

The first simulations done were to confirm the relevance of the results and mechanism described in Reference [45] and [46] for both polarizations at oblique incidence with 2-dimensionally patterned gratings. Figure 6.7 shows the reflectivity as a function of wavelength and grating thickness for a grating composed of square-cross section pillars of crystalline silicon tiled on a square lattice with angle of incidence of 45° and polar angle set so that the plane wave is incident along one of the grating vectors with $n_{med} = 1$. The general characteristics of reflectivity match those for one-dimensional grating structures illuminated by a single polarization of light. First, for long wavelength light with $\lambda_0 > 1800\ nm$, there are weak Fabry-Perot resonance reflection peaks and valleys as the grating thickness changes. The shortest wavelength light ($\lambda_0 < 500\ nm$) is strongly absorbed, so the reflectivity in this region is low. For shorter intermediate wavelengths (500 $nm \leq \lambda_0 \leq 1000\ nm$, the feature size of the grating is larger than the incident wavelength giving higher order diffraction. Thus, the specular reflectivity is low. Finally, the target high-contrast grating behavior is achieved for λ_0 between 1000 nm and 1800 nm where the lowest order guided modes of the grating layer are accessible. Here, modal

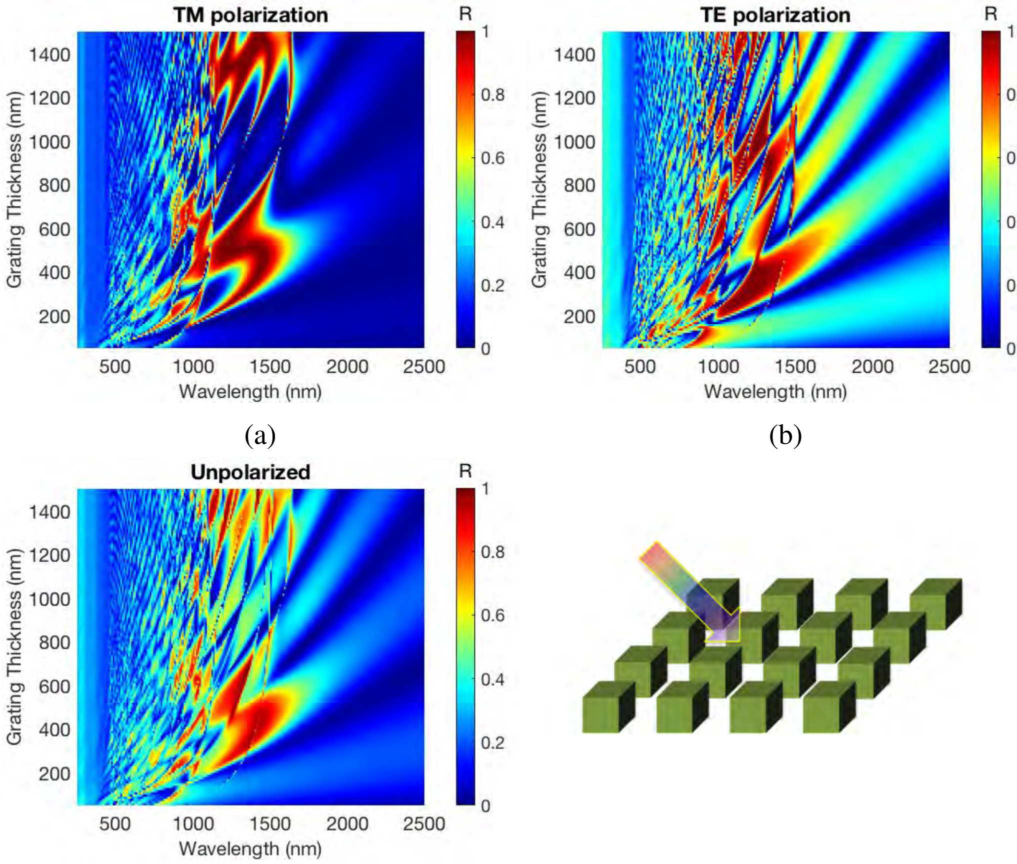

(a) (b)

(c) (d)

Figure 6.7: (top) Grating reflectivity for TM and TE polarized illumination on square cross-section pillars arrayed on square lattice with silicon grating material and $n_{med} = 1$. (bottom) Grating reflectivity for unpolarized light and grating schematic showing 45° broadband illumination.

interference gives high specular reflectivity.

Oblique incidence creates problems of having degenerate grating coupling vectors and polarization sensitivity, decreasing reflection peaks. As seen in Figure 6.7c, the strong reflection regions for TM and TE polarization do not overlap fully, giving lower maximum reflectivity values for unpolarized light. Higher refractive index of the grating medium decreases these effects since light is refracted toward normal incidence as it passes into the grating making the large range of angles in the medium have more similar reflectivity. The magnetic field intensity in a c-Si grating with air medium at the resonance wavelengths at normal incidence and 45° incidence, shown in Figure 6.8, indicate that in both cases similar modes are excited within the grating element. The longer wavelength resonance is an electric dipole resonance and the shorter wavelength resonance a magnetic dipole. The proximity of these two

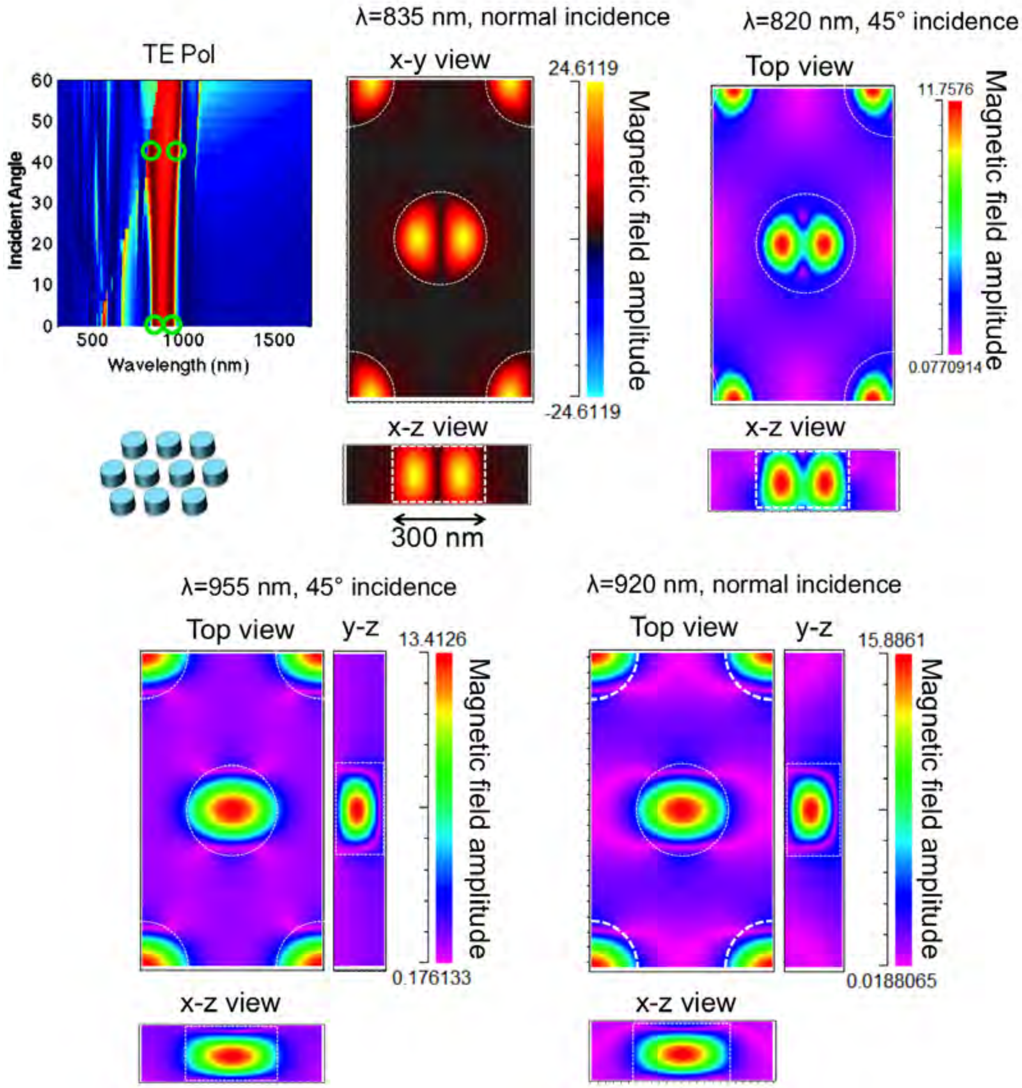

Figure 6.8: Magnetic field profiles of a grating on resonance illuminated by TE polarization light at normal incidence and 45° incidence showing very similar modes excited in both cases. The longer wavelength resonances appear to be electric dipole resonances while the shorter wavelength resonance is due to a magnetic dipole.

resonances gives the broadband reflectivity desired with $\frac{\Delta\lambda}{\lambda} \approx 0.11$. To additionally mitigate polarization sensitivity and the washing out of the top-hat reflection profile, we opted to use higher rotational symmetry gratings with circular cross-section pillars on a hexagonal lattice. There are five independent parameters for this grating geometry. The two materials parameters which can be changed are the refractive indices of the grating and of the medium. The three geometrical parameters are grating thickness (or pillar height), fill fraction (the percentage of the grating area

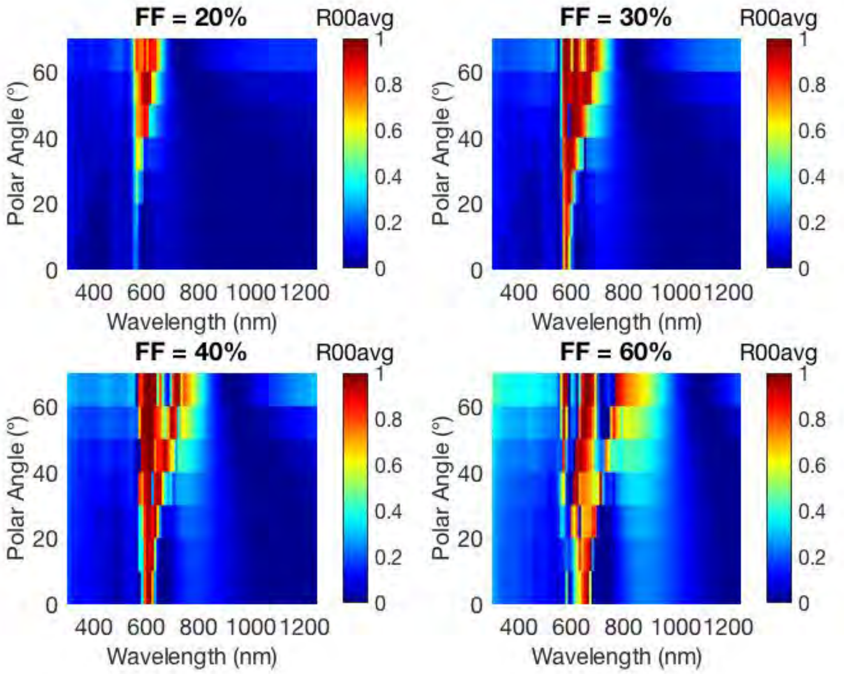

Figure 6.9: Reflectivity of AlSb high-contrast grating with $n_{med} = 1.5$, period=250 nm and grating thickness $t_g = 250\ nm$ for varying grating thickness fill fraction FF.

occupied by the grating material), and period of the grating. The fill fraction and period together fix a certain pillar diameter. (Any two among grating periodicity, fill fraction, and pillar diameter are independent.) Each of these parameters were varied to explore the grating design space for this geometry.

Figure 6.9 shows the reflection spectra for unpolarized illumination as a function of incident light versus incident polar angle for four different values of fill fraction with fixed period. The higher symmetry grating has more uniform reflection between the two polarizations as seen in >90% reflection peaks which require aligned reflection bands for the two polarizations. This AlSb grating in $n = 1.5$ medium shows that for low fill fractions, the reflection band is not strong, dipping below 40% near normal incident. As the fill fraction increases, the peak reflectivity goes up and the reflection bandwidth increases. Finally, at high fill fractions coupling between the adjacent grating elements leads to more complex mode profiles and reflectivity. The combination of parameters for FF=30% and FF=40% give quite desirable reflectivity. The effects of varying grating thickness are shown in Figure 6.10. Below the optimal thickness, the reflection modes present are dispersive and weak. At the optimal thickness, the modes interfere to produce an angle independent reflection. As the thickness increases beyond the optimal thickness, the two modes,

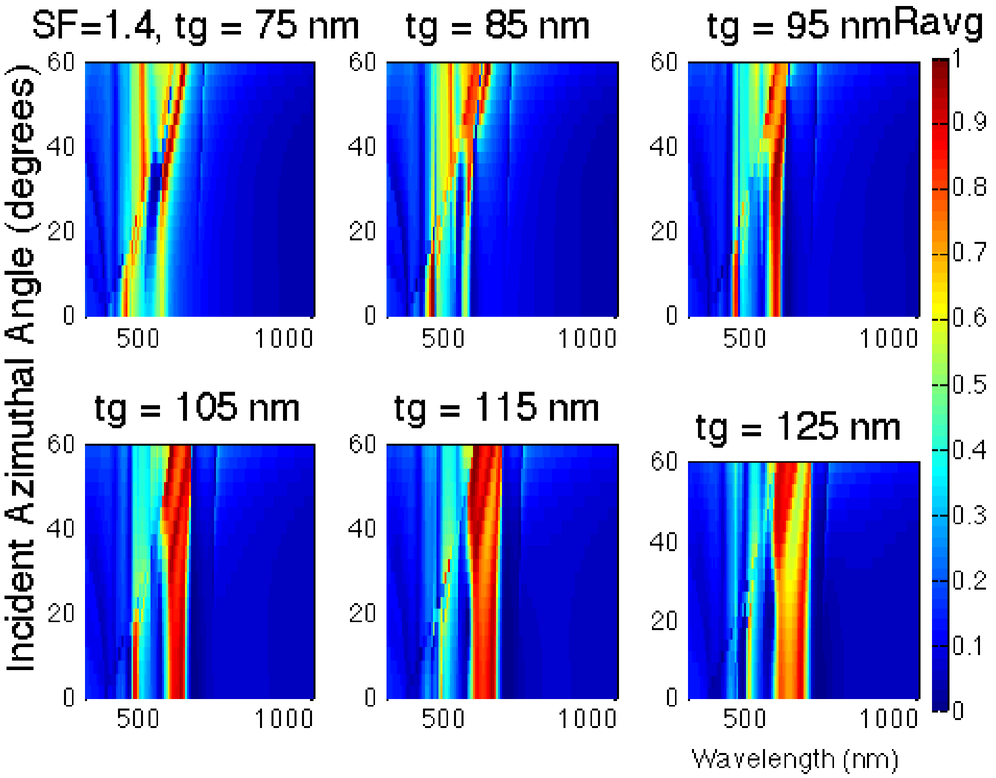

Figure 6.10: Reflectivity of a Si high-contrast grating with n_{med} = 1, pillar diameter=210 nm and FF=22.7% for varying grating thickness t_g.

shown above to be electric and magnetic dipole modes, move further apart giving a broader reflection band with lower reflectivity.

Maxwell's equations are scale invariant. Thus, for the wavelength range that refractive index of the grating material does not change much, the structure can be scaled up in all three-dimensions and show the same reflectivity for a proportionally scaled up wavelength. Figures 6.11b-d show the reflection characteristics of a silicon in air grating scaled up in size by factors of two, three, and four in each linear dimension. There are minor differences attributable to the dispersion of the silicon grating material over this wavelength range. Doing a fine re-optimization of the grating parameters around the scaled-up values could result in better performance.

Grating Materials

Grating materials must have high refractive index and low absorption throughout the wavelength range of interest. The inverse relationship of high bandgap energy materials having lower refractive index make this challenging. The refractive index and bandgap of a variety of possible materials are given in Figure 6.12. For

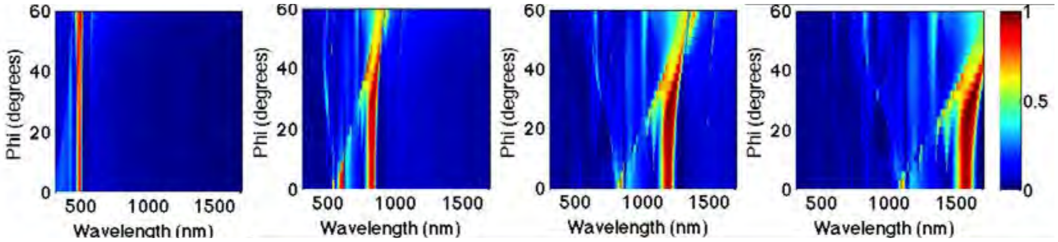

Figure 6.11: Reflectivity of silicon grating in n=1 medium with (left to right): $a = 300nm$, $r_{disk} = 75nm$, $tg = 70nm$; $a = 600nm$, $r_{disk} = 150nm$, $t_g = 140nm$; $a = 900nm$, $r_{disk} = 225nm$; $a = 1200nm$, $r_{disk} = 300nm$, $t_g = 280nm$. ©2015 IEEE

a photovoltaic technology to be scalable, as discussed in Chapter 5, cost is a key factor. Thus, materials such as TiO_2 or polycrystalline silicon, which have cheaper component elements and are widely used industrially, are preferable. Materials such as aluminum antimonide and gallium phosphide in contrast are typically epitaxially grown by slower processes on expensive substrates for precise electrical properties. Good optical properties can be achieved with lower quality materials, so it is possible that viable fabrication routes for polycrystalline or amorphous GaP or AlSb exist which give sufficient optical quality without high-cost growth. Generally, however, as a material moves from high-quality single crystalline to polycrystalline to amorphous structure, sources of deleterious absorption increase. From a performance standpoint, higher refractive index gives greater angle-independence and higher peak reflectivity as long as the reflection peak is at an energy below the material bandgap. Bandgap of 3.1 eV or greater would give low absorption across the entire solar spectrum of interest. The highest refractive index materials such as Si, AlSb, and GaP and common materials with high bandgap energy such are TiO_2 and silicon carbide are the most interesting candidates for high-contrast gratings based on these criteria.

The most favorable grating media are run-of-the-mill transparent dielectrics which are low cost and already validated for use in photovoltaics such as glass and PMMA with $n_{med} \approx 1.5$. However since refractive index contrast is a key factor in HCG performance, I also simulate media with $n_{med} = 1$ and $n_{med} = 1.2$. The former can be approximated by patterning "mushroom caps" of high refractive index by etching an undercut into the substrate material. Likewise $n_{med} = 1.2$, while not accessible with bulk materials, can be approximated using highly porous materials. Long-term practical concerns for porous and undercut etched materials include mechanical robustness and potential for dust and moisture incursion, both of which can be detrimental to the lifetime of a photovoltaic system that needs to maintain its

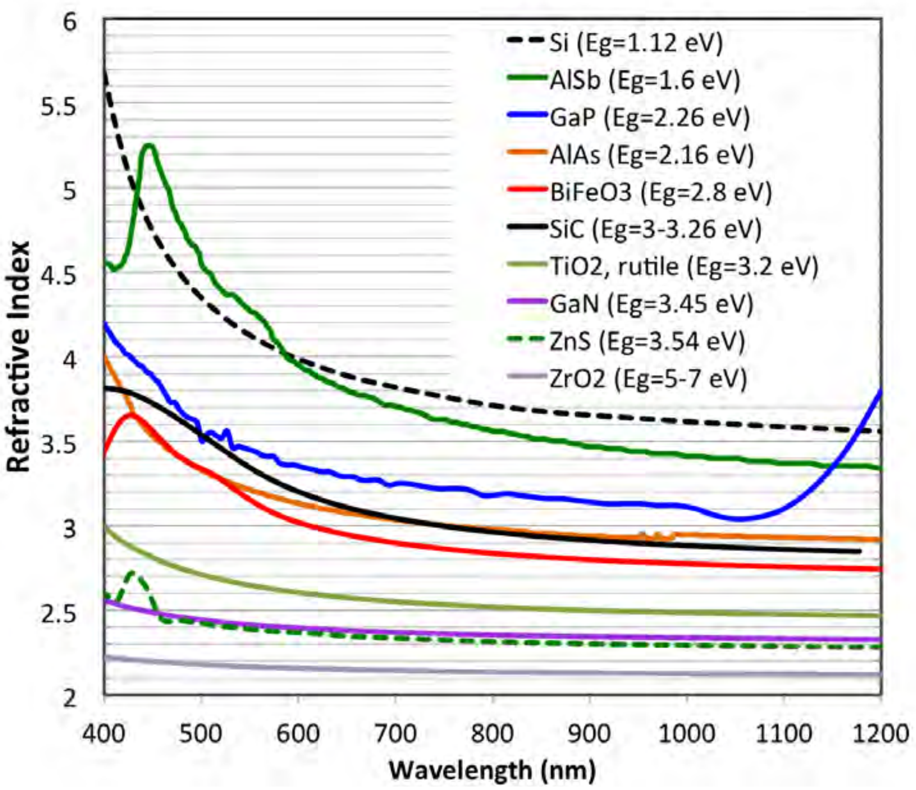

Figure 6.12: Candidate high-refractive index materials for high-contrast gratings.

performance over a 25-year timescale. Table 6.1 details the grating materials and media simulated. For the $n_{med} \approx 1.5$ simulations, a geometrical parameter sweep was done to quickly target a promising parameter range for high reflectivity. This included simultaneously sweeping grating thickness ($t_g = 50-1000\ \mu m$), fill fraction ($FF = 10\% - 90\%$) for a fixed value of grating period, or grating width ($P \approx 250\ nm$ for AlSb, 240 nm for Si, and $width = 200\ nm$ for GaP). Specular and total reflectivity, direct and total transmission and grating absorption were simulated as a function of wavelength and incident polar angle. Even using an optimistic refractive index of $n_g = 2.7$ for TiO_2, the index contrast is too low to give angle-independent reflection bands (Figure 6.13). The data shown are representative of the best results from a thorough parameter sweep of grating fill fraction and thickness. The reflection features which are present vary in wavelength significantly as the angle of incidence changes. In addition to this high dispersion, the index contrast is not high enough to obtain high reflectivity across incident angles. A more realistic refractive index for TiO_2 deposited by methods suitable for large volume production is between 2.2 and 2.5. Thus, we must seek higher index materials or lower index media for our applications.

	Si	GaP	n=2.7	n=2.4	SiN	AlSb	AlAs
air	x	x	x	x			
n=1.2							
n=1.5	x	x	x	x		x	x
air/n=1.5 interface	x	x			x		

Table 6.1: High-contrast grating simulated materials combinations

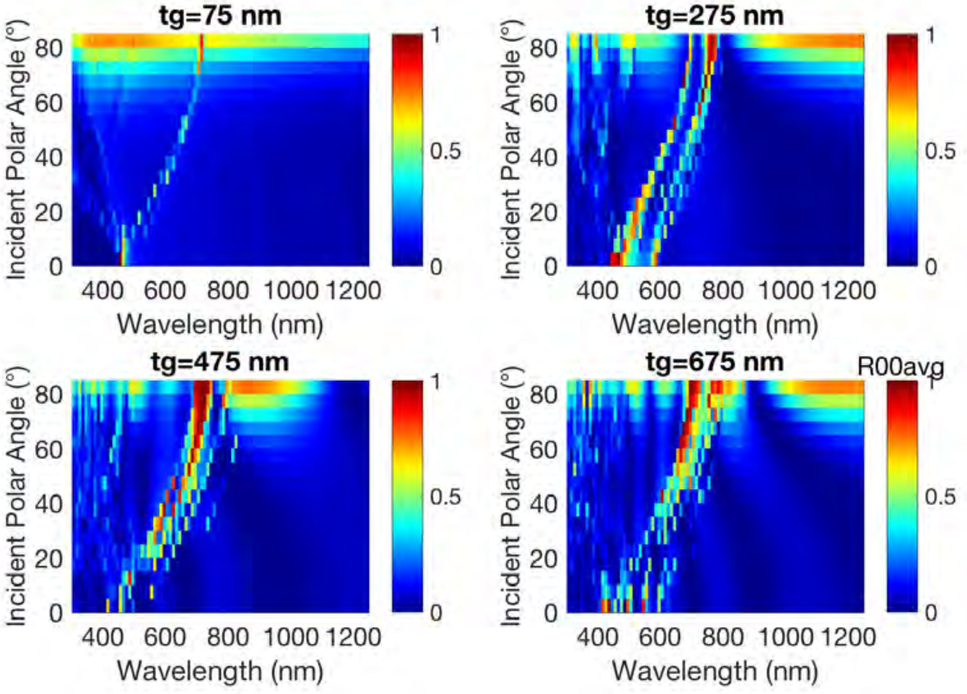

Figure 6.13: Reflectivity as a function of wavelength and incident angle for a dispersionless and lossless grating material with $n_g = 2.7$ and $n_{med} = 1.5$. Reflection bands are dispersive and do not have high reflectivity for a width range of angles.

Figure 6.14 shows the best polar angle-averaged reflectivity simulated for AlSb, Si and GaP gratings in an n=1.5 medium. Fully angle-averaged peak reflectivity will be slightly lower due to azimuthal angle variation which gives lower reflectivity for plane waves oriented along directions of lower density in the grating (e.g., oriented in the direction lying between the two lattice vectors). GaP shows higher transmission across the out-of-band regions due to its higher bandgap ($E_g = 2.26\ eV$). It absorbs strongly, however, below its bandgap. AlSb has an indirect bandgap at 1.6 eV with its direct bandgap strong absorption onset around 2.2 eV. Its refractive index of 4 at 600 nm gives better peak reflectivity making it a promising candidate material as well. Silicon has a comparable refractive index around 3.8 at 600 nm but has a

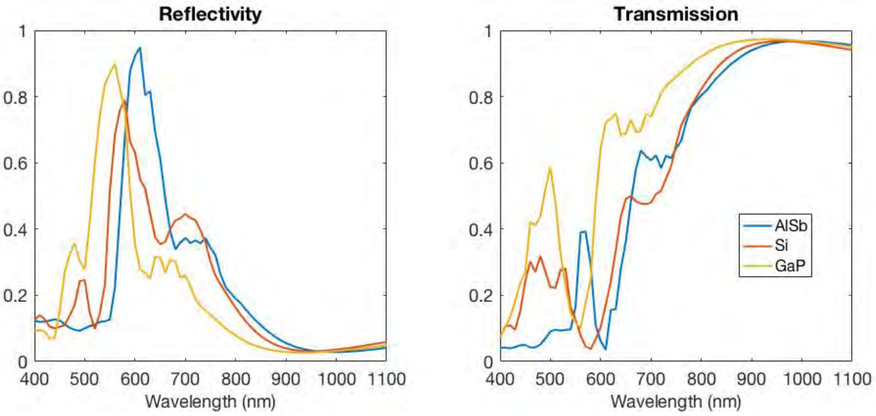

Figure 6.14: Hemispherically angle-averaged reflectivity and transmission as a function of wavelength for AlSb, Si and GaP gratings in $n_{med} = 1.5$.

lower energy indirect bandgap giving higher absorption at the target luminescence wavelength band.

The final steps in optimizing these best results are to repeat simulation for a higher the number of harmonics, include azimuthal angle variation, and fine-tune the values of the grating thickness, period, disk diameter, and fill fraction for optimization performance. This process will likely improve in-band reflectivity and out-of-band transmission slightly. The target specs of >99% in-band reflectivity and >97% out-of-band transmission, however, remain elusive. We need to consider more significant design changes to approach these values.

One option for increasing peak reflectivity above what is seen in Figure 6.14 is to stack more than one HCG. Figure 6.15a shows the reflection of a single GaP grating as well as two GaP gratings one on top of the other with a large enough spacer to treat the reflectivity of each layer independently. Thus we can estimate the reflectivity change due to the additional layer with $\Delta R = T \times R \times T$ where the additional reflectivity comes from light which transmits through the first grating, gets reflected off the second and finally gets transmitted through the first grating again, back into the waveguide. As seen from this expression, unfortunately stacking pays off less and less as the initial reflectivity gets better. 70% reflectivity becomes 76% while 90% becomes 91%. Even worse, the shoulder of reflectivity for long wavelengths is at the peak for highest ΔR, increasing unwanted reflectivity from 30% to 45%. Stacking two layers close enough to give optical coupling between them may give different results and remains to be simulated.

Another possibility is exploiting total internal reflection by placing the grating near an air-glass interface. Figure 6.15b shows the same GaP grating fully immersed in an $n = 1.5$ medium with an air interface a half-wavelength ($\frac{\lambda_0}{2*n_{med}}$) away from the grating. The grating is embedded a half-wavelength deep just inside the glass semi-infinite half at an air-glass interface. The presence of the interface increases in-band peak reflectivity when illuminated from the glass side by $14.5\%_{abs}$. Thus the angle-averaged reflectivity experienced by photons luminesced by the quantum dots improves. Additionally the reflectivity for long wavelength illumination which must pass through the front and back mirrors to reach the underlying silicon solar cell remains largely unchanged. Unless long wavelength light is scattered as it enters the waveguide, the angular spread when it reaches the back mirror from the waveguide will the the same refracted angle spread as it has upon entering from the air side. The relevant reflectivity value will thus still be the lower air-side reflectivity. Incorporating the total internal reflection of an air-glass interface also requires using a different criterion for selecting the best HCG grating. Total internal reflection perfectly reflects light outside the escape cone of 41° for an air/n=1.52 interface. Thus, the HCG's performance now depends on its performance up to 41° not a full hemispherical angle-average.

HCG in the Polyhedral Specular Reflector

Individual HCG have reflection bands too narrow to serve as band-stop filters for the PSR, let alone longpass filters. As described above stacking gratings is not very effective at increasing already high peak reflectivity. However, it is more effective at widening a reflection band. Figure 6.16 shows two of the seven filter bands approximated by silicon in air gratings from those shown in Figure 6.11 along with some intermediate scaling. For band 5 requiring reflectivity between 874 nm and 1078 nm, two gratings are stacked with the combined reflectivity given by $R_{total} = R_1 + T_1^2 \times R_2$ and combined transmission by $T_{total} = T_1 \times T_2$. The base gratings do not have high reflectivity at 45°, so the structure would need reoptimization for the appropriate angle range. In the images shown peak reflectivity occurs around 20° angle of incidence. As seen in Figures 6.9b and 6.9c, near-unity, polarization averaged reflectivity can be obtained at 45°. The biggest downside of stacking gratings is diminished transmission for out-of-band wavelengths. It remains to be seen how much benefit can come from adding antireflection layers onto the resonant structures to cut down on long-wavelength Fabry-Perot reflections. In all likelihood, these gratings would find better applications in alternate spectrum splitting geometries than the PSR for which out-of-band transmission efficiency is

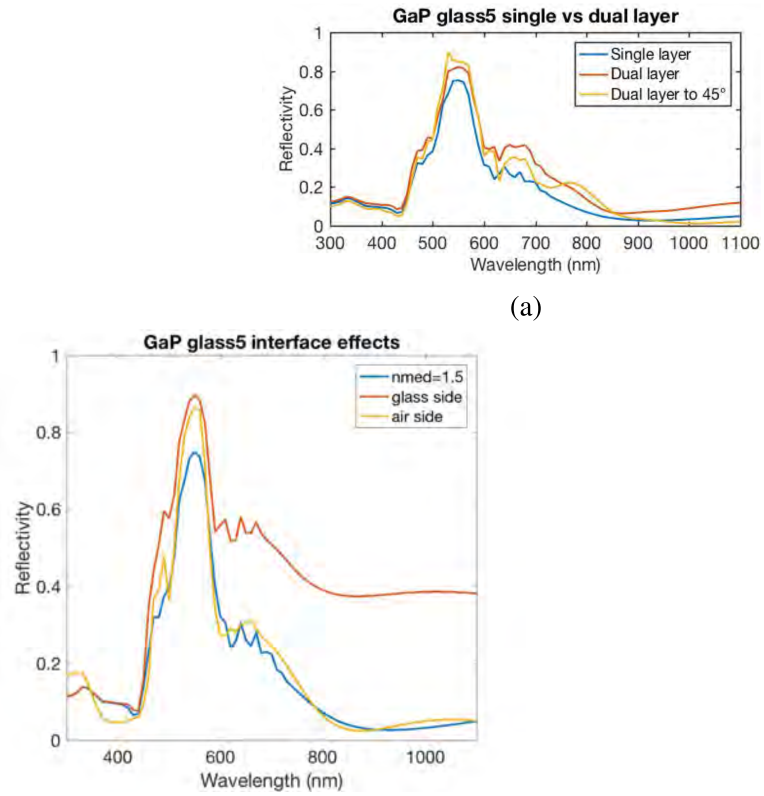

(a)

(b)

Figure 6.15: Reflectivity of (left) GaP HCG near an air/glass interface, and (right) GaP pillars topped with SiN HCG.

very important to overall performance.

Evaluating mirrors for tandem luminescent solar concentrator

While peak reflectivity is easy to read off a plot, assessing the performance of one mirror against another in the trade-off between high in-band reflectivity and high out-of-band transmission benefits from a more holistic metric. Thus, a figure of merit to weight different spectral and angular ranges by their relative importance is needed. Ultimately, I sought a figure of merit to closely approximate the amount of power converted in the correct cell. In order to estimate this, first, I assume that solar illumination over a 60° half-angle cone of angles of totally diffuse light can be collected. Thus, I can integrate the mirror reflectivity over this range, angle averaging the output of my RCWA simulations $R(\theta_{ext}, \phi, \lambda)$ to get

$$R_{ext}(\lambda) = \int_0^{\frac{2\pi}{3}} R(\theta_{ext}, \phi, \lambda) \cos\theta \sin\theta d\theta d\phi, \tag{6.3}$$

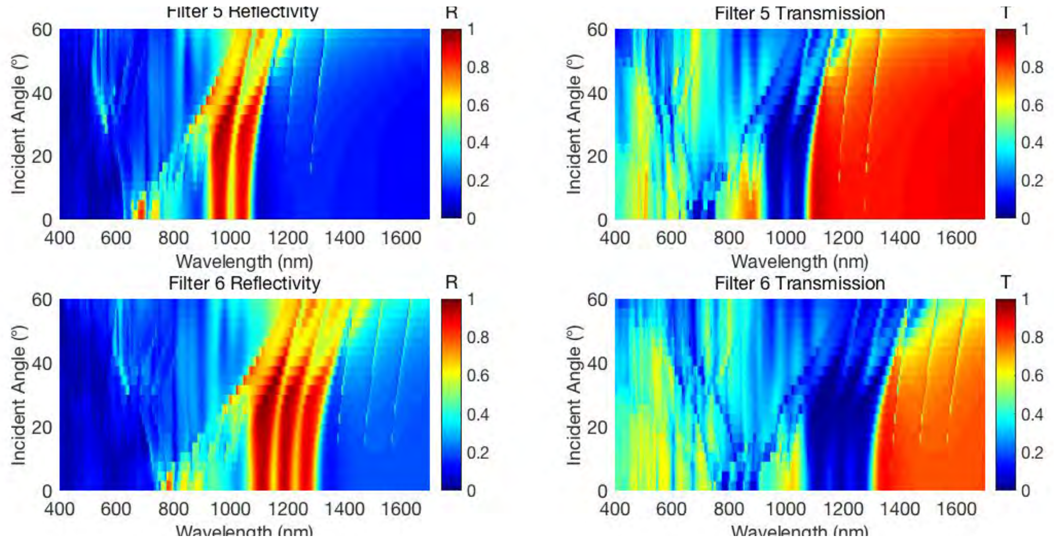

Figure 6.16: Multiple silicon in air structures stacked to generated wider reflection bands for PSR band 5 on top and band 6 on the bottom.

where ϕ is the polar angle and θ the azimuthal angle and R mirror reflectivity. I similarly angle average the mirror from the waveguide side, this time considering uniform illumination from the quantum dots embedded in the LSC waveguide over a whole hemisphere to get

$$R_{int}(\lambda) = \int_0^{\pi} R(\theta_{int}, \phi, \lambda) \cos\theta \sin\theta d\theta d\phi. \tag{6.4}$$

Now I define the Figure of Merit (FoM) to be

$$FoM(n) = \frac{P_{Si} + P_{InGaP}(n)}{Incident\ Solar\ Power}, \tag{6.5}$$

where the silicon cell power P_{Si} is defined as

$$Power = V_{OC} \times FF \times \sum_i Flux(\lambda_i) \tag{6.6}$$

using properties of a high quality silicon heterojunction HIT cell to give the open circuit voltage $V_{OC} = 730\ mV$, fill fraction $FF = 0.8$, and short-circuit current is estimated as

$$J_{SC,Si} = \sum_{\lambda=525\ nm}^{1200\ nm} AM1.5G(\lambda_i) \times T_1(\lambda_i) \times T_2(\lambda_i) \times EQE_{Si}(\lambda_i),$$

where I only consider the wavelength range 525 nm to 1200 nm which is the intended band for the silicon cell. $EQE_{Si}(\lambda_i)$ is for a Kaneka HIT cell from [51]. The flux reaching the silicon cell is defined as the sum of the AM1.5 global reference

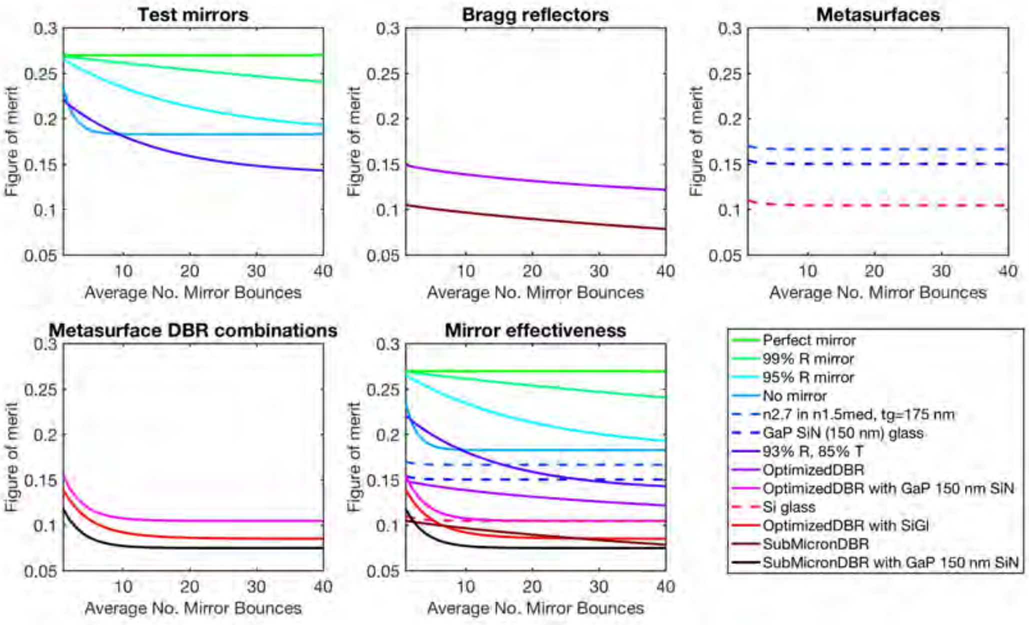

Figure 6.17: Figure of merit for Tandem Luminescent Solar Concentrator design for ideal filters, Bragg reflectors, high-contrast gratings, and combinations of the two as a function of average mirror bounces.

spectrum transmitted through mirrors 1 and 2 and converted by the silicon cell. The power of the InGaP top cell P_{InGaP} is a function of the average number of mirror bounces which depends on the architecture of the device. Analogous to P_{Si}, it is defined by equation 6.6 as the product of InGaP voltage ($V_{OC} = 1.4\ V$), fill fraction ($FF = 0.85$), and current, calculated by

$$Flux_{InGaP}(\lambda_i) = PL_{QD}(\lambda_i) \times (R_{int}(\lambda_i))^n, \tag{6.7}$$

where n is the average number of mirror bounces and the quantum dot photoluminescence $PL_{QD}(\lambda_i)$ is

$$PL_{QD}(\lambda_i) = \left(\sum_{\lambda=300\ nm}^{525\ nm} T_1(\lambda_i) \times AM1.5G(\lambda_i) \times A_{QD}(\lambda_i) \right) \times \frac{PL(\lambda_i)}{\sum_i PL(\lambda_i)}. \tag{6.8}$$

The quantum dot absorption is assumed to be a step function with no absorption for $\lambda > 525\ nm$ and perfect absorption at shorter wavelengths. The InGaP cell is additionally assumed to have unity EQE. All short wavelength photons which are transmitted through the top mirror are thus assumed to be absorbed by a quantum dot and re-emitted. The final factor in equation 6.8 redistributes the total number of re-emitted photons into the experimental photoluminescence spectrum of the quantum dots. The number of these re-emitted photons which are retained in the waveguide and thus converted by the InGaP cell depends on the mirror reflectivity over the wavelength range of photoluminescence and the average number of mirror bounces.

The results of this figure of merit can vary based on the choices of the open-circuit voltage, FF and EQE of each cell as well as the cutoff off wavelength and average number of mirror bounces. Using the listed assumptions above and calculating the FoM as a function of mirror bounces from 1 to 40 for a number of mirrors, we get Figure 6.17. Our Monte Carlo modeling performed by David Needell indicates the number of mirror bounces is a strong function of mirror quality with as many 500 bounces for a perfect mirror or as few as three for a poor mirror. As indicated in the figure, neither the currently designed Bragg reflectors optimized by Colton Bukowsky or the HCG discussed in this chapter or combinations of the two have yet to reach the performance of notional mirrors with flat angle-independent reflectivity in-band and transmission out-of-band. In general, the FoM shows that metasurfaces cannot be use for the top mirror as the absorption of light between 400 nm and 525 nm for silicon, AlSb and GaP is too high. This is evident in the flat Figure of Merit for the HCG metasurfaces which do not change as a function of the number of mirror bounces. The power converted by the metasurface mirror TLSC comes primarily from light transmitted directly to the silicon cell, since the light that should be collected in the top cell which would be susceptible to loss at higher numbers of mirror bounces is largely absorbed by the HCG. In contrast, the DBR mirrors have high in-band reflectivity and no short-wavelength absorption (they assume lossless dielectric materials). Thus even after a large number of mirror bounces, the FoM value has not plateaued. There is still energy collected by the InGaP which could be lost at a higher number of mirror bounces. However the value of the FoM is low due to low out-of-band transmission to the underlying silicon cell.

Among the DBR/HCG combinations shown with a DBR front mirror and a HCG back mirror, the current results seem to combine the worst qualities of each mirror. The trapped photoluminescence is lost in under 10 mirror bounces while the transmission to the silicon cell is low. In part this is due to the reflection peaks of the HCG being centered at slightly too short wavelength to be well aligned with the quantum dot photoluminescence as shown in Figure 6.15. This is a matter of slightly scaling up the gratings to give reflectivity that is well aligned with the emission peak. Additionally, prioritizing transmission to the silicon cell can give the combinations higher efficiency potential. This path is the one we are currently pursuing for this design.

6.3 Summary and Next Steps

Rigorous coupled-wave analysis simulations of reflection and transmission efficiency of high-contrast gratings were done. The gratings were evaluated for use as spectrum-splitting optical elements in the PSR and the Tandem Luminescent Solar Concentrator. These high-refractive index, near-subwavelength-scale gratings were shown to have relatively angle-independent reflection peaks. Paired Fano resonances give breadth to the reflection band. The bandwidth, peak reflectivity and angle insensitivity improved with higher refractive index contrast between the grating material and medium. Also, lower extinction coefficient gave higher peak reflectivity. Thus AlSb and GaP are optimal materials with low absorption in the visible range and high refractive indices. Finally, it was shown that stacking additional patterned layer and placement of air interfaces could improve performance. Appropriately sized reflection bandwidths are possible for the longer wavelength spectral bands of the PSR. The out-of-band transmission however is not high enough to give high device efficiency. Achieving at least >85% in-band reflectivity and >90% out-of-band transmission overall from the stacked gratings would enable 40% module efficiency. The much more stringent requirements for the narrower band tLSC filters require >99% in-band reflectivity and >97% out-of-band transmission to improve upon the conversion efficiency of a high quality silicon cell alone. The absorption in materials with high enough refractive index for promising reflectivity was shown to be too much to use the current high-contrast gratings as the front mirror in a tLSC. The best-to-date peak angle-averaged reflectivity is 95% for an AlSb grating in n=1.5 medium with about 80% long wavelength transmission.

Next steps targeting incremental improvements should focus on increasing peak reflectivity, decreasing long wavelength Fresnel reflections and short-wavelength diffraction. In part this should be done by finely adjusting the geometrical parameters of gratings. Additionally, simulations should be repeated at a higher number of modes to get refined results. Application of optimization methods to reduce manual parameter sweeps could significantly speed up this design process. Slight randomization in position of grating elements should be tested. It is possible that this would decrease higher order diffraction efficiency (i.e., short wavelength diffraction) without strongly interfering with the lower order resonances which create the high-contrast grating reflection band. Studies should be done permuting the shape of the individual grating resonators to check the effect. Literature has shown high sensitivity of HCG reflection to grating element shape such as sharp corners. While it is likely to be low especially as the refractive index goes up, this check is necessary as fabrication errors are inevitable, and an understand of their influence on performance should be quantified for large scale applications. Fabrication of gratings alongside further simulation to confirm tolerances is also necessary. Among other factors, evaluating whether or not the AlSb indirect bandgap of $E_g = 1.6\ eV$ is absorbing too in the photoluminescence wavelength range for effective use is a high priority. Finally, improvements to the figure of merit include accounting for the fact that not all light hitting a solar cell in an average low DNI environment is uniformly distributed across a hemisphere. This assumption penalizes our technology significantly compared to the peak efficiency of a conventional solar cell which is measured at normal incidence and should be addressed.

To move the needle on HCG performance for spectrum splitting photovoltaics, different geometries and materials combinations need to be explored. Moving beyond variations of the single patterned layer grating, geometrical combinations of HCG and DBR remain to be fully explored. For example, while optically independent stacked HCG layers did not give improvements, optically coupled stacked layers have not been explored. In overall device design, high-contrast gratings should be explored as light trapping optical elements in traditional luminescent solar concentrators. Such single junction luminescent solar concentrator designs would reduce the transmission problem to just that of short wavelength light rather than both short and long wavelength light. Additionally, short-wavelength transmitted diffracted orders could be less of a problem in such an architecture. Finally, it remains to be investigated whether there are scalable methods of obtaining GaP and AlSb and if there are any materials use concerns for AlSb for large-scale deployment in photovoltaics.

Regarding materials selection, ways of exploiting high refractive index TiO_2 in an air medium seems to be the last hope for possibly using HCG as a front mirror or a short wavelength filter in a photovoltaic application. Design work remains to be done with this material pair. Any future materials innovation in transparent, high refractive index material could be fruitfully applied to high contrast gratings, for example development of a germanium carbide with high refractive index and lower bandgap than SiC. Regarding high efficiency luminescent solar concentrator work, a key enabling technology will be high quantum yield, near infrared quantum dots.

This would enable both higher efficiency single junction and tandem luminescent solar concentrators by allowing the trapped and thus rejected spectral window to move away from the peak of the solar spectrum. A quantum dot with emission near λ=800 nm would pair well with GaAs solar cells, either as a single junction or as a top junction for a tandem cell with silicon.